Infrared Spectroscopy and Inelastic Recoil Dynamics of OH Radicals in Complexes with *ortho*- and *para*-D_2

Michael W. Todd, David T. Anderson, and Marsha I. Lester*

Department of Chemistry, University of Pennsylvania, Philadelphia, Pennsylvania 19104-6323

Received: February 22, 2000; In Final Form: April 26, 2000

The rotationally resolved infrared (IR) spectrum of D_2−OH in its ground electronic state has been obtained in the OH overtone region at 1.4 μm via IR−ultraviolet (UV) action spectroscopy. The pure OH overtone and combination bands involving intermolecular bending excitation were observed. The experimental spectrum was compared with IR transition frequencies computed from ab initio theory for *o*-D_2−OH and *p*-D_2−OH. The state-selective IR excitation of D_2−OH also serves to initiate inelastic and/or reactive scattering dynamics between the D_2 and OH partners under restricted initial orientation conditions. Time- and frequency-resolved measurements of the OH (v = 1) fragments from vibrational predissociation showed that vibrationally activated D_2−OH is short-lived and that the D_2 fragment is vibrationally excited as a result of an efficient near-resonant vibration-to-vibration energy transfer process. The remaining 350 cm^{-1} of available energy is disposed primarily as rotational excitation of OH. The OH fragments also exhibit a striking lambda-doublet preference, revealing alignment of the unpaired pπ orbital with respect to the OH rotation plane that changes with the intermolecular state selected. The results are consistent with half-collisions that sample different restricted angular regions of the OH + D_2 potential energy surface for each of the initially prepared states.

I. Introduction

Reactive and inelastic collisions of hydroxyl radicals play an important role in the complex dynamics of atmospheric and combustion environments.[1,2] The OH + H_2 system is a prototypical example of such an interaction and, as a result, has become a benchmark system for four-atom reaction dynamics[3−8] and inelastic scattering studies.[9−14] This laboratory has focused on half-collision studies of OH with H_2, which are initiated by vibrational activation of H_2−OH complexes that have been stabilized in a shallow attractive well in the entrance channel to reaction.[15−18] The half-collision dynamics start from a restricted range of orientations between the OH and H_2 partners, thereby yielding complementary information to full collision studies that average over all possible initial geometries. Vibrational excitation of either the OH or H_2 diatom within H_2−OH provides sufficient energy to surmount the barrier to reaction or, alternatively, to break the weak intermolecular bond. Vibrationally activated H_2−OH can therefore lead to two different sets of products, H + H_2O or OH + H_2, depending on whether the system decays by reaction or vibrational predissociation (inelastic scattering). Both of these channels may contribute to the rate of decay of vibrationally activated H_2−OH. The reactive decay channel may also influence the inelastic scattering dynamics, as some nonreactive encounters may be "frustrated" attempts at chemical reaction.[19−22]

In the past few years, the weakly bound H_2−OH complex has been examined by a number of theoretical and experimental methods.[13,15−18,23−29] The bound states and infrared (IR) spectrum of H_2−OH in its ground electronic state were predicted from quantum mechanical calculations that were based on a high-level ab initio potential energy surface developed by Clary, Werner, and co-workers (MCKW).[13] These calculations treated the open-shell nature of the OH $X\ ^2\Pi$ + H_2 system explicitly, but did not take into account the possibility of reaction. Nevertheless, the theoretical predictions provided a near-quantitative guide to understanding the experimental IR spectrum of *ortho*-H_2−OH in the OH overtone stretch region.[28,29] The rotationally resolved IR spectrum has been shown to access the ground intermolecular state of *o*-H_2−OH ($\nu_{OH} = 2$) as well as excited bending states that extend out to the OH $X\ ^2\Pi$ (v = 2) + *o*-H_2 $X\ ^1\Sigma_g^+$ dissociation limit. Stimulated Raman studies in the H_2 stretch fundamental region revealed a single rovibrational feature that probes the ground intermolecular state of *o*-H_2−OH ($\nu_{H_2} = 1$).[17]

Experiments have also been performed to elucidate the lifetime of vibrationally activated *o*-H_2−OH and the product state distributions of the OH and H_2 fragments following mode-specific excitation to the $\nu_{OH} = 2$ and $\nu_{H_2} = 1$ states.[15−18,29] Krause and Clary have carried out complementary time-dependent wave packet calculations of the vibrational predissociation dynamics.[15,18] A surprising degree of mode selectivity was observed, with both experiment and theory yielding predissociation lifetimes for $\nu_{H_2} = 1$ that are at least an order of magnitude shorter than those for $\nu_{OH} = 2$. Much of the mode selectivity has been attributed to an increase in the vibrational predissociation rate for *o*-H_2−OH ($\nu_{H_2} = 1$), although an enhancement in reaction rate upon H_2 vibrational excitation[30,31] may also contribute to the shorter lifetime.

Although a significant body of research has been conducted on H_2−OH, less is known about the D_2−OH isotopomer.[15,24,25] Particularly useful in this regard would be analogous spectroscopic, dynamical, and theoretical studies of D_2−OH in its ground electronic state; such studies are the primary objectives of this paper. The D_2−OH complex is of interest for many reasons. First, the bound states and IR spectrum of D_2−OH probe the same potential energy surface as examined by H_2−OH, thereby providing an additional set of observables for direct

* Corresponding author. E-mail: milester@sas.upenn.edu. Fax: (215) 573-2112.

10.1021/jp000685p CCC: $19.00
Published on Web 06/23/2000

comparison between experiment and theory. Second, the nuclear spin statistics of D_2 make detection of both *o*- and *p*-D_2−OH complexes more favorable when using *normal*-D_2 (*n*-D_2) carrier gas, whereas only the *o*-H_2−OH complex has been observed with *n*-H_2. This enables the spectroscopic and dynamical properties of OH radicals in complexes with *o*-D_2 ($j_{D_2} = 0$) and *p*-D_2 ($j_{D_2} = 1$) to be compared. Third, a near-resonant vibration-to-vibration (V−V) energy transfer channel is open in the vibrational predissociation of D_2−OH ($\nu_{OH} = 2$) that significantly reduces the translational energy release to products. Therefore, the product state distribution is anticipated to be highly sensitive to the characteristics of the underlying potential energy surface.

Preliminary results on the predissociation dynamics of D_2−OH ($\nu_{OH} = 2$) have been presented elsewhere.[15] The vibrational predissociation channel proceeds via the transfer of one quantum of vibrational excitation from OH to D_2 in a V−V process

$$D_2{-}OH\ (\nu_{OH} = 2) \rightarrow D_2\ (v = 1, j_{D_2}) + OH\ (v = 1, j_{OH})$$

with an exothermicity of ∼350 cm^{-1}. This reaction can be contrasted with the vibrational predissociation of H_2−OH ($\nu_{OH} = 2$), where the energy released from one quantum of OH vibration is transferred solely into product rotation and translation in a V−R,T process

$$H_2{-}OH\ (\nu_{OH} = 2) \rightarrow H_2\ (v = 0, j_{H_2}) + OH\ (v = 1, j_{OH})$$

with an exothermicity of ∼3350 cm^{-1}. The significantly reduced energy available to the fragments in the case of D_2−OH ($\nu_{OH} = 2$) restricts the OH ($v = 1$) products to low rotor states ($j_{OH} \leq 9/2$), whereas much more extensive rotational excitation of the OH ($v = 1$) fragments ($j_{OH} \leq 23/2$) is detected for H_2−OH ($\nu_{OH} = 2$).[15,16] The near-resonant V−V process provides a facile decay channel for D_2−OH ($\nu_{OH} = 2$).[15]

This paper presents a more comprehensive look at the predissociation dynamics of D_2−OH ($\nu_{OH} = 2$) following state-selective preparation in four different initial states. The initial states are prepared by IR excitation in the OH overtone stretch region. Quantum calculations of the bound states of *o*- and *p*-D_2−OH are carried out to furnish IR transition frequencies for comparison with experiment. In addition, the bound state wave functions are examined to provide physical insight into the relative orientation of the D_2 and OH partners within the complex for specific initial states. Finally, the time evolution and complete product state distribution (rotational and fine structure) of the OH ($v = 1$) fragments are obtained, revealing a striking lambda-doublet effect that changes with the initial state selected. These changes are correlated with the restricted angular regions of the intermolecular potential energy surface that are sampled by the different initial states of D_2−OH.

This paper is organized as follows: Section II describes the IR pump−ultraviolet (UV) probe technique that was employed for frequency- and time-resolved studies of D_2−OH. Section III gives a brief description of the bound rovibrational states of D_2−OH derived from quantum calculations on the MCKW ab initio potential. Section IV presents the experimental IR overtone spectrum and the theoretically predicted transition frequencies for D_2−OH. The rates for appearance of OH fragments and their product state distributions are also measured for specific intermolecular states of D_2−OH ($\nu_{OH} = 2$). Section V explores the characteristics of the initially prepared D_2−OH states, the reasons for rapid decay upon OH vibrational activation, and the origins of the alignment observed for the unpaired pπ orbital of the OH fragments. Conclusions and plans for future work are outlined in Section VI.

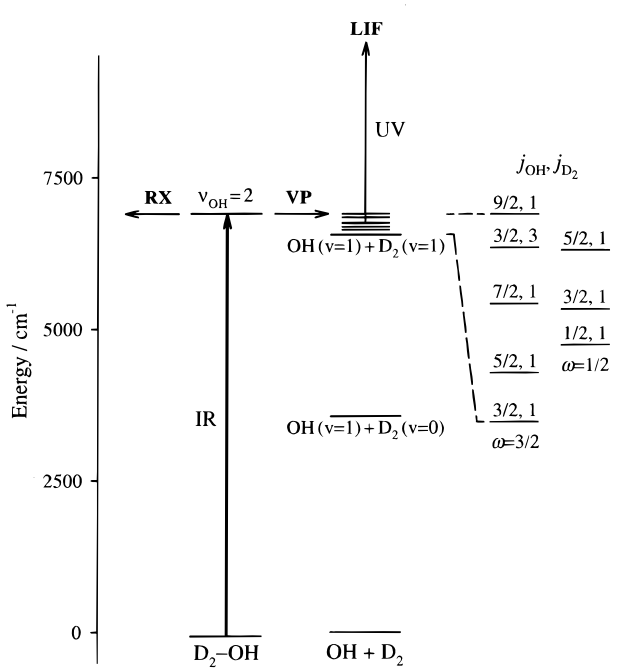

Figure 1. IR pump−UV probe scheme used to investigate the IR spectrum, lifetime, and predissociation dynamics of D_2−OH ($\nu_{OH} = 2$). The IR laser prepares D_2−OH with two quanta of OH stretch and provides sufficient energy to surmount the barrier to reaction (RX) or, alternatively, to rupture the weak intermolecular bond via vibrational predissociation (VP). The UV laser probes the OH ($v = 1$, j_{OH}) fragments of predissociation via laser-induced fluorescence (LIF). D_2−OH ($\nu_{OH} = 2$) can predissociate through an efficient vibration-to-vibration energy transfer process that leaves the D_2 fragment vibrationally excited. The 350 cm^{-1} of excess energy can then be disposed as rotational excitation of the OH and/or D_2 fragments or translational recoil. The enlargement details the energetically accessible product rotational channels (j_{OH}, j_{D_2}) for *p*-D_2 ($v = 1$) with OH ($v = 1$) in its ground ($\omega = 3/2$) and excited ($\omega = 1/2$) spin−orbit states.

II. Experimental Section

The present experiments use an IR pump−UV probe scheme to probe the IR spectrum, lifetime, and OH product state distribution of vibrationally excited D_2−OH complexes. As illustrated in Figure 1, the IR pump laser prepares D_2−OH with two quanta of OH stretch and possible intermolecular vibrational excitation. The vibrationally activated D_2−OH ($\nu_{OH} = 2$) complex contains more than sufficient energy to break the weak intermolecular bond via vibrational predissociation (VP) or undergo chemical reaction (RX). The UV probe laser monitors the OH ($v = 1$) products from vibrational predissociation on the OH A−X 0−1 transition, resulting in a laser-induced fluorescence signal (LIF). Three types of measurements are performed: (1) Scanning the IR pump laser with the UV probe laser fixed on an OH product transition produces an IR action spectrum. (2) Varying the time delay between the IR and UV laser pulses gives the time evolution of the OH products and ultimately the lifetime of D_2−OH ($\nu_{OH} = 2$). (3) Tuning the UV probe laser through various OH A−X 0−1 lines, while keeping the IR laser fixed on a specific rovibrational transition of the D_2−OH complex, yields the OH ($v = 1$) product state distribution. The experimental procedures are elaborated next.

As described in detail previously,[24,25] D_2−OH complexes are produced in a pulsed supersonic expansion. Nitric acid is entrained in a 30% *n*-D_2/He balance gas mixture at 150 psi

backing pressure and expanded through a pulsed valve. The OH radicals are then generated by 193 nm photolysis of the gas mixture within a quartz capillary tube (1 cm length, 300 μm i.d.) that is affixed to the faceplate of the pulsed valve. The photolysis position and backing pressure are selected to optimize formation of D_2-OH complexes as well as vibrational and rotational cooling of OH radicals. The pulsed valve is also cooled to ~0 °C with a Peltier cooling element, which further enhances complexation.

The IR pump laser is the idler output of an injection-seeded Nd:YAG pumped β-barium borate (BBO) optical parametric oscillator (OPO) laser (Continuum Sunlite, 10 Hz, 7 mJ/pulse, 4 ns, 0.12 cm^{-1}), which operates in the OH overtone region at ~1.4 μm. The UV probe is the 350 nm output of a XeCl excimer pumped dye laser (Lambda Physik FL2002, 20 Hz, 1.5 mJ/pulse, 20 ns, 0.20 cm^{-1}) with Exalite 351 dye. The IR and UV beams are counter-propagated through the vacuum chamber and focused to a ~1 mm^2 spot size, intersecting the supersonic expansion ~15 mm downstream from the exit of the capillary tube. The IR beam is also retro-reflected back into the interaction region using a spherical mirror (50 cm focal length). The mirror has a 5-mm hole in its center to allow the UV probe laser to pass through the mirror and into the vacuum chamber. The retro-reflected beam provides ~30% more IR power in the interaction region.

The OH LIF signal is collected with a lens assembly f/1 and imaged onto a photomultiplier tube (PMT), which is positioned perpendicular to the laser and supersonic expansion axes. A spherical mirror (f/1) is also placed on the opposite side of the interaction region to collect fluorescence from a greater solid angle and reflect it back onto the PMT. A long-pass filter is used to block 193 nm scatter, and a band-pass filter centered at 308 ± 20 nm ensures that only OH A−X 0−0 fluorescence is detected. The fluorescence signal is preamplified before being captured by a boxcar, integrated over a 200-ns gate, and transferred to a laboratory computer.

The lasers are synchronized such that the IR pump laser (10 Hz) is present for every other UV probe laser pulse (20 Hz), with the UV laser typically arriving in the interaction region 30 ns after the IR pulse. For lifetime measurements, the delay between the IR and UV lasers is stepped in 1-ns increments from −50 to 100 ns using an EG&G digital delay generator. On alternating gas pulses (20 Hz), the LIF signal arising from the UV laser *only* (IR off) or that resulting from the *combination* of the IR + UV (IR on) is collected. Typically, 100 IR on and 100 IR off signals are averaged at each frequency step (or time interval). The difference, IR on − IR off, results in active background subtraction at a 10-Hz repetition rate.

In addition, the IR overtone spectrum of D_2-OH was obtained using a fluorescence depletion technique, in which the UV probe laser is fixed on a previously characterized electronic transition of D_2-OH in the OH A−X 1−0 region. Here, the UV probe laser is the ~280 nm output of a frequency-doubled Nd:YAG pumped dye laser (Continuum ND6000, 20 Hz, 30 mJ/pulse, 7 ns, 0.20 cm^{-1}) operating with Rhodamine 6G dye. The resultant LIF signal is collected with the same active background subtraction scheme employed in action spectroscopy, but with the subtracted signal divided by the LIF signal arising from the UV laser only (IR off) and multiplied by 100 to convert to a percent depletion.

The idler output of the OPO was calibrated by recording a photoacoustic spectrum of water.[32] In addition, relative frequency markers were obtained as the IR pump laser was scanned by passing the signal output from the OPO (~471.5 nm) through an etalon (4.17 mm, 0.812 cm^{-1} FSR). The UV probe laser frequency was calibrated using well-known OH A−X transitions.[33]

A few experiments were conducted with a recently acquired higher resolution IR pump source, namely, a single-mode potassium titanyl phosphate (KTP)-based OPO (Continuum Mirage 3000, 10 Hz, 7 mJ/pulse, 4 ns). The laser bandwidth at 1.4 μm was determined by measuring the breadth of individual rovibrational lines in the photoacoustic spectrum of water (17.5 Torr) at 300 K.[32] The line shapes were well reproduced by a Lorentzian function with a full width at half-maximum (fwhm) of 0.04 cm^{-1}, which provides an upper limit for the IR pump laser bandwidth.

III. Bound State Calculations

Before presenting the IR spectroscopic data and analysis for D_2-OH, it is useful to provide theoretical background based on four-dimensional (intermolecular) quantum calculations of the bound rovibrational states of D_2-OH. Previously, Clary and co-workers calculated the bound states and IR spectrum of H_2-OH using a variational finite basis approach and their MCKW ab initio potential energy surface.[13] The calculated rovibrational energies served as an important guide in this laboratory for assigning the experimental IR spectrum of H_2-OH.[28,29] However, no calculations have been reported for the D_2-OH isotopomer. Because the intermolecular bound states in these types of weakly bound species can be isotopomer dependent, we carried out equivalent bound state calculations for D_2-OH using Clary's computer codes.[13,23] The eigenvalues and eigenfunctions were calculated with no angular momentum decoupling approximations and explicitly treating the open-shell character of OH.

For a description of the bound state calculations, the reader is referred to refs 13 and 23. Only the numerical details specific to the D_2-OH calculations are presented here. The reduced mass of D_2-OH is 3.2586 amu and the rotor constant of D_2 is 29.91 cm^{-1}.[34] The primitive stretching eigenfunctions were composed of 80 equally spaced Gaussians between $R = 2$ and 30 a_0. The primitive angular basis is truncated by restricting the maximum values to $j_{OH} = 11/2$ and $j_{D_2} = 7$. The eigenfunctions of the primitive stretching and angular basis sets are initially determined separately. These primitive eigenfunctions are then used to construct the product basis set that generates the final energy levels. For D_2-OH, the final basis consisted of a product of 30 stretch and 75 angular primitive eigenfunctions. The resultant bound states are given in Table 1 for total angular momentum $J = 1/2$ to 5/2, with their energies defined relative to the OH ($j_{OH} = 3/2$, $\omega = 3/2$) + D_2 ($j_{D_2} = 0$ or $j_{D_2} = 1$) asymptotes for *o*- and *p*-D_2-OH, respectively. Here, j_{D_2} and j_{OH} denote the angular momenta associated with the D_2 and OH diatoms, respectively, and ω labels the spin-orbit state of OH through the projection of j_{OH} on the OH axis $\mathbf{r}_{OH}$. The energies of the lowest bound states are converged to within 1 cm^{-1}, whereas their relative energies are stable to <0.1 cm^{-1}.

As discussed previously for H_2-OH,[13,23,29] the barriers to internal rotation of D_2 and OH in D_2-OH are not sufficient to quench (mix j_{D_2} or j_{OH}) the internal rotational motions associated with the diatoms, making it appropriate to model the complex as two weakly interacting rigid rotors. The overall rotation of the complex and the intermolecular stretch are treated in a pseudo-diatomic limit. The calculated rovibrational energy levels are labeled by the rigorous quantum numbers for total angular momentum J and total parity p (+ or −), as well as by the approximate quantum numbers j_{D_2}, j_{OH}, ω, K, and n_{str}. Here, K

TABLE 1: Energies[a] (cm^{-1}) for Selected Bound States of *o*- and *p*-D_2−OH with Total Angular Momentum $J \leq 5/2$ and + or − Total Parity (*p*)

n_{str}[b]	K[b]	*p*	$J = 1/2$	$J = 3/2$	$J = 5/2$
			o-D_2−OH		
0	3/2	+		−43.0	−40.9
		−		−43.0	−40.9
0	1/2	+	−33.8	−30.8	−31.2
		−	−32.8	−32.8	−28.5
0	−[c]	+	−26.5	−26.8	−23.7
		−	−27.4	−25.6	−25.3
0	−[c]	+		−24.0	−20.3
		−		−23.5	−21.2
1	3/2	+		−8.2	−6.1
		−		−8.2	−6.1
			p-D_2−OH		
0	1/2	+	−60.1	−58.5	−55.9
		−	−60.4	−58.0	−56.7
0	5/2	+			−55.0
		−			−55.0
0	−3/2	+		−50.0	−48.5
		−		−50.2	−48.1
0	−1/2	+	−49.2	−46.6	−44.0
		−	−48.9	−47.0	−43.5
0	3/2	+		−42.1	−39.8
		−		−42.1	−39.7
0	1/2	+	−38.2	−35.9	−33.7
		−	−38.0	−36.3	−33.1
0	−[c]	+	−28.9	−27.3	−24.6
		−	−29.0	−27.2	−24.9
0	−3/2	+		−19.0	−16.6
		−		−19.1	−16.6
1	1/2	+	−18.7	−15.7	−13.5
		−	−18.9	−15.2	−14.3
1	5/2	+			−13.3
		−			−13.2

[a] Energies of *o*-D_2−OH bound states are defined with respect to the OH ($j_{OH} = 3/2$, $\omega = 3/2$) + *o*-D_2 ($j_{D_2} = 0$) asymptote, whereas *p*-D_2−OH bound states are defined with respect to the OH ($j_{OH} = 3/2$, $\omega = 3/2$) + *p*-D_2 ($j_{D_2} = 1$) asymptote that lies 59.8 cm^{-1} higher in energy. [b] The rovibrational states are labeled by approximate quantum numbers for intermolecular stretch (n_{str}) and the body-fixed projection of *J* on the intermolecular axis (*K*). The approximate n_{str} and *K* quantum numbers are determined by inspection of the wave function. [c] *K* assignment is not possible because of strong Coriolis coupling.

denotes the body-fixed projection of *J* on the intermolecular axis **R** and can also be expressed as $k_{D_2} + k_{OH}$, the sum of the body-fixed projections of j_{D_2} and j_{OH}. Further, n_{str} can be used to label the intermolecular stretching mode. There are also two high-frequency intramolecular modes, ν_{OH} and ν_{D_2}. The experimental measurements involve excitation of the OH overtone, so that $\nu_{OH} = 2 \leftarrow 0$. However, in the quantum calculations, the D_2 and OH bond lengths are held fixed at their $\nu_{OH} = 0$ and $\nu_{D_2} = 0$ values.

The intermolecular potential lifts the m_j spatial degeneracy of j_{D_2} and j_{OH} in the complex, creating a $(2j_{D_2} + 1)(2j_{OH} + 1)$ manifold of *K* states involving bending motion (internal rotation) of the constituent monomers. These intermolecular states differ in the relative orientation of OH and D_2 within the complex. The ordering and energy spread across the manifold of angular states is directly related to the anisotropy of the intermolecular potential.[23] The *K* labels shown in Table 1 are identified by examination of the coefficients of their eigenfunctions after transforming to a body-fixed frame of reference. Coriolis interactions can couple states with different *K* ($\Delta K = \pm 1$), causing shifts in their energies and breaking down the goodness of the *K* quantum label. When Coriolis coupling is weak, as is the case for many of the lowest energy *K* states, the *K* label provides information on the vibrationally averaged 'structure' of D_2−OH in that intermolecular state.

The change in the intermolecular potential arising from the orientation of the unpaired pπ orbital of OH, which can lie either within or perpendicular to the D_2−OH plane, causes a splitting between states of + and − parity ($\Delta_p = E^+ - E^-$) with the same total angular momentum *J*. The magnitude and sign of Δ_p varies enormously for different intermolecular states of D_2−OH, as can be seen in Table 1. Using perturbation theory, Green and Lester showed that Δ_p scales with $(J + 1/2)$ for a $|K| = 1/2$ state and with $(J - 1/2)(J + 1/2)(J + 3/2)$ for a $|K| = 3/2$ state.[35] Therefore, the computed *J* dependence of Δ_p also provides indirect evidence of the *K* label for a given state.

The intermolecular energy level pattern for *o*-D_2−OH is very similar to those of Ar−OH and *p*-H_2−OH.[13,23,36] The four lowest energy *K* states are derived predominantly from $j_{D_2} = 0$ and $j_{OH} = 3/2$. The ground intermolecular state of *o*-D_2−OH is bound by only 43 cm^{-1} (D_0) and is predicted to be $K = 3/2$, with a negligibly small parity splitting. The first excited intermolecular bending state of *o*-D_2−OH lies ~11 cm^{-1} higher in energy and is identified as a $K = 1/2$ state with a relatively large parity level splitting. The next two intermolecular bending states are strongly mixed by Coriolis coupling such that a *K* assignment is not very meaningful. The first excited intermolecular stretch ($K = 3/2$) is predicted to lie ~35 cm^{-1} to higher energy in close proximity of the dissociation limit.

The intermolecular energy level pattern for *p*-D_2−OH is more complicated because of the unquenched angular momenta associated with the *p*-D_2 ($j_{D_2} = 1$) and OH ($j_{OH} = 3/2$) subunits. The ground intermolecular state of *p*-D_2−OH is bound by 60 cm^{-1} (D_0) and is predicted to be a $K = 1/2$ state with a relatively large parity splitting. The lowest excited intermolecular bending states are identified at ~5 cm^{-1} ($K = 5/2$) and ~10 cm^{-1} ($K = -3/2$) to higher energy, both with small parity splittings. The next excited intermolecular bending state at ~11 cm^{-1} is a $K = -1/2$ level with a large parity splitting that is comparable in magnitude but opposite in sign to the ground state. More highly excited intermolecular bending states extend throughout the bound region of the potential. The first excited stretching state is predicted to appear at ~42 cm^{-1}. The higher stretching frequency for *p*-D_2−OH as compared with *o*-D_2−OH is consistent with the greater binding energy for *p*-D_2−OH.

Infrared transition frequencies for *o*- and *p*-D_2−OH can be predicted from the bound state energies (Table 1) for comparison with experimental data. Far-infrared transition frequencies are first calculated using $\Delta J = 0, \pm 1$ and $p' \neq p''$ selection rules. These transitions involve rovibrational excitation of intermolecular modes only. Near-infrared transition frequencies can then be obtained by adding on an estimate for the band origin, 6972.1 cm^{-1}, of the pure OH overtone transitions for *o*- and *p*-D_2−OH (assumed to be the same) as discussed in Section IV. A. The latter step assumes that the dipole of the complex is identical in orientation with the OH monomer and the intermolecular potential is unaffected by OH stretching excitation.[13,23] The theoretically predicted transition frequencies will be compared with the experimentally observed IR overtone spectrum for D_2−OH in the next section.

Line strength factors have not been computed for the IR transitions of the D_2−OH isotopomer. Rather, we assume that the line intensities in the IR spectrum of D_2−OH follow the trends predicted by Miller et al. (and experimentally observed) for H_2−OH.[13] Strong Q-branch lines are expected to dominate the rotational structure of intermolecular vibrational bands with much weaker P/R lines. Combination bands will generally

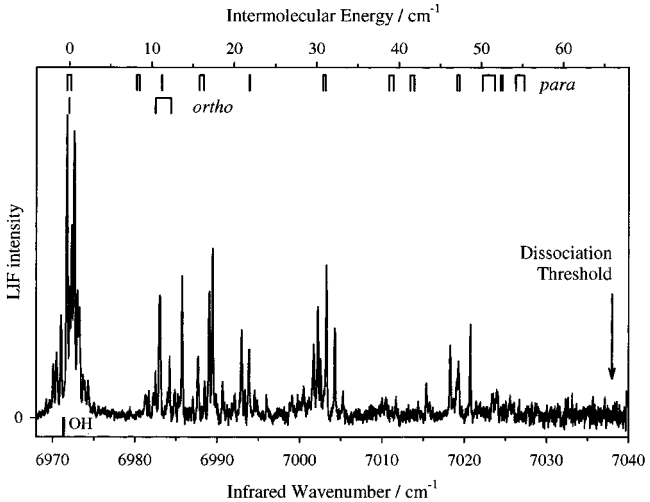

Figure 2. Rotationally resolved IR overtone spectrum of D_2-OH obtained with the UV probe laser monitoring the OH (v = 1) products of vibrational predissociation on the OH A−X 0−1 $Q_1(9/2)$ transition. The pure OH overtone band is the cluster of lines centered about 6972.1 cm^{-1}, which appears near the OH monomer v = 2←0 transition (shown on abscissa). Transitions to higher energy are combination bands involving the simultaneous excitation of two quanta of OH stretch and intermolecular bending modes. The theoretically predicted Q-branch transitions for *p*-D_2-OH (*para*) and *o*-D_2-OH (*ortho*) are shown as ticks above the spectrum. The top axis represents increasing intermolecular energy of D_2-OH ($\nu_{OH} = 2$) from its ground state (0 cm^{-1}) to the OH $X\ ^2\Pi$ (v = 2) + D_2 dissociation limit.

involve intermolecular bending vibrations, because excited intermolecular stretching states are not expected to have appreciable intensity.

For *o*-D_2-OH, intermolecular transitions should follow a $\Delta K = 0, \pm 1$ selection rule, by analogy with ArOH and *p*-H_2-OH.[13,23,36,37] As a result, the most intense features in the near-IR spectrum of *o*-D_2-OH are anticipated to be transitions to the ground $K = 3/2$ and excited $K = 1/2$ intermolecular states at ~0 and 11 cm^{-1} of intermolecular excitation. For *p*-D_2-OH, the infrared transition strength is likely to be spread over many of the bending states extending out to the dissociation threshold due to Coriolis coupling effects, as found for *o*-H_2-OH.[13,23] The lowest possible Q-branch transitions that are expected to be observable in the near-IR spectra of *o*- and *p*-D_2-OH are shown as tick marks in Figure 2.

IV. Results and Analysis

A. Infrared Overtone Spectrum and Interpretation. The IR overtone spectrum of D_2-OH has been obtained in the vicinity of the OH monomer v = 2←0 transition[38] at 6971.3 cm^{-1} and is displayed in Figure 2. This spectrum was recorded via action spectroscopy with the UV probe laser set to detect the OH (v = 1) fragments from vibrational predissociation on the OH A−X 0−1 $Q_1(9/2)$ transition. The probe transition was empirically selected based on the magnitude of the OH fragment LIF signal. The IR spectrum of D_2-OH was also recorded using other UV probe transitions via action spectroscopy as well as by the fluorescence depletion method. As will be discussed in Section IV.C, the relative peak intensities and signal-to-noise ratio in the IR spectra vary enormously depending on which UV probe transition is chosen, yet the frequencies of the peaks in the D_2-OH IR spectrum remain unchanged. The IR action spectrum obtained with the probe laser on the OH $Q_1(9/2)$ line (Figure 2) yields the best signal-to-noise ratio and thus is used to illustrate the main features of the D_2-OH IR spectrum.

The dominant feature in the D_2-OH IR overtone spectrum is a cluster of rotationally resolved lines near 6972 cm^{-1}. This cluster of strong lines appears close to the OH monomer Q(3/2) overtone transition, indicated on the abscissa at 6971.3 cm^{-1}, but not observed because of the selectivity imposed by action spectroscopy. Scans to lower energy revealed no lines below 6969 cm^{-1}. As a result, this cluster is attributed to rovibrational lines of the pure OH overtone band of D_2-OH with no intermolecular excitation. Additional features appear at higher energy beginning at ~6981 cm^{-1} and are associated with rovibrational lines from combination bands involving the simultaneous excitation of OH stretch and intermolecular bending modes. The intermolecular energy of these vibrational levels is shown by the top axis of Figure 2, which originates from the center-of-gravity of the pure overtone band at 6972.1 cm^{-1}.[39] The intermolecular energy axis also reveals that the D_2-OH IR action spectrum extends over 50 cm^{-1}, consistent with the ground-state binding energy determined via electronic spectroscopy[24] ($D_0 \sim 66$ cm^{-1}) and predicted by theory ($D_0 \sim 60$ cm^{-1} for *p*-D_2-OH). An arrow at 7038 cm^{-1} marks the dissociation threshold anticipated from the experimental D_0 value.

Transitions from both *o*-D_2-OH and *p*-D_2-OH may contribute to the observed IR spectrum for D_2-OH. Although only one form of H_2-OH has been observed to date, specifically *o*-H_2-OH, both *ortho* and *para* forms of D_2-OH are expected to be observable with *n*-D_2 carrier gas. This expectation follows from previous experimental observations for the closed shell analogue H_2/D_2-HF, where both *o*- and *p*-D_2-HF were detected even though only *o*-H_2-HF was observed.[40,41] The greater binding energy predicted for *p*-D_2-OH (60 cm^{-1}) as compared with *o*-D_2-OH (43 cm^{-1}) could lead to preferential formation of *p*-D_2-OH in the supersonic expansion. In *n*-D_2, however, *o*-D_2 ($j_{D_2} = 0, 2, ...$) is present in twice the abundance of *p*-D_2 ($j_{D_2} = 1, 3, ...$) because of nuclear spin statistical weights. The larger abundance of *o*-D_2 will increase the probability of *o*-D_2 + OH collisions and the likelihood of *o*-D_2-OH formation, and should lead to comparable amounts of *o*- and *p*-D_2-OH being produced in the supersonic expansion. Thus, spectroscopic transitions arising from both *o*- and *p*-D_2-OH may be observable.

Our interpretation of the D_2-OH IR spectrum begins with a comparison of the experimentally observed features with theoretical predictions of the IR transition frequencies, because theory provided an important guide in assigning the H_2-OH IR spectrum. The theoretically predicted IR transitions for *o*- and *p*-D_2-OH are shown as ticks in Figure 2; only Q-lines of the lowest *J* with + and − parity are displayed. For *o*-D_2-OH, just two bands centered at 0 and 11 cm^{-1} of intermolecular energy are expected to have appreciable IR transition strength, as discussed in Section III. For *p*-D_2-OH, the pure overtone and bending combination bands extending over the entire bound state region should have significant IR intensity (Section III). As a result of the theoretical predictions, we anticipate that *p*-D_2-OH and *o*-D_2-OH will have overlapping rotational band structure in the pure overtone region. The Q-lines of the *o*-D_2-OH pure overtone band (with negligible parity splittings) may overlap the Q-branch region of the *p*-D_2-OH band (with measurable parity splittings), and P/R lines from *o*-D_2-OH may account for some of the weaker lines at the edges of the band. In addition, rovibrational transitions from both *o*- and *p*-D_2-OH may contribute to the combination band at ~11 cm^{-1} of intermolecular energy. Here, Q-lines of the *o*-D_2-OH combination band (with sizable parity splittings) may appear in the

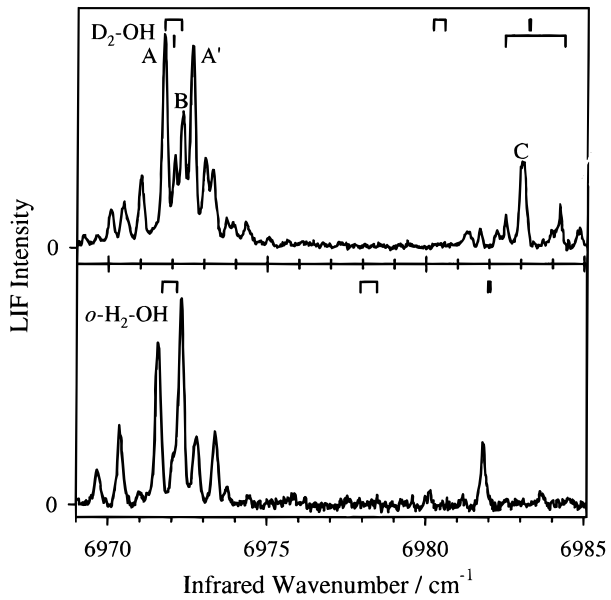

Figure 3. An expanded view of the low energy portion of the IR overtone spectrum for D_2-OH (Figure 2) and that previously recorded for H_2-OH (ref 16). The theoretically derived IR transition frequencies for *p*- and *o*-D_2-OH as well as *o*-H_2-OH are shown as ticks above the spectra. Four different initial states of D_2-OH, accessed by IR excitation of features A, A′, B, and C, are the focus of dynamical studies. See Figure 2 for explanation of ticks.

vicinity of Q-lines from the *p*-D_2-OH band (with overlapping parity components). The additional D_2-OH features observed at higher energy are most likely due to *p*-D_2-OH exclusively.

Next, the IR spectrum of D_2-OH is compared with the previously recorded IR spectrum of H_2-OH.[16,28,29] The general features of the IR overtone spectrum of *o*-H_2-OH (see Figure 4 in ref 29) are very similar to the IR overtone spectrum of D_2-OH shown in Figure 2. Expanded views of the lower energy portions (6969−6985 cm^{-1}) of the spectra are shown in Figure 3. The lower energy region is the focus of our comparison of the two nuclear spin states as transitions arising from both *o*- and *p*-D_2-OH are anticipated for D_2-OH, whereas the IR spectrum of H_2-OH has been attributed solely to *o*-H_2-OH.[29] The IR spectrum of *o*-H_2-OH shown in Figure 3 was recorded by action spectroscopy with the UV probe laser fixed on the OH A−X 0−1 $Q_1(23/2)$ transition.[16] The theoretically derived IR transition frequencies for *o*-H_2-OH as well as those for *p*- and *o*-D_2-OH are shown as ticks above the experimental spectra. (Note that some of the predicted transitions, e.g. $K = -3/2 \leftarrow 1/2$, are not observed in either the *o*-H_2-OH or D_2-OH experimental spectra.)

The absolute frequencies of the lines in the H_2-OH and D_2-OH spectra are distinctly different from one another, yet there are clear similarities between the two spectra. The pure OH overtone bands of both isotopomers appear near 6972 cm^{-1} (the band origin for *o*-H_2-OH is at 6971.9 cm^{-1}). Most of the lines in the pure overtone band of *o*-H_2-OH have been assigned as Q-branch transitions. A large parity splitting causes the + and − parity components of the Q-branch lines to be split further apart from one another with increasing *J*, resulting in the relatively symmetric contour in the pure overtone band of *o*-H_2-OH. The lowest P/R-branch lines are barely observable at the edges of the band. A similar rotational band structure is expected for the pure overtone of *p*-D_2-OH. Thus, many of the strong central lines of the pure overtone band of D_2-OH can be attributed to the + and − parity components of Q branch lines of *p*-D_2-OH, with weaker transitions at the edges of the band likely due to P/R-branch lines.

There are also some important differences between the IR spectra of the two isotopomers (Figure 3). In particular, there are more lines in the pure overtone band of D_2-OH compared with that in *o*-H_2-OH. These extra lines are unlikely to stem from additional rotational structure in the pure overtone band of *p*-D_2-OH compared with *o*-H_2-OH. The bound state calculations indicate that the rotational energy level spacings within the lowest $K = 1/2$ intermolecular level are comparable for *o*-H_2-OH and *p*-D_2-OH. This result is somewhat surprising given the change in the reduced mass on isotopic substitution, and reflects a significant reduction in the intermolecular separation distance for D_2-OH compared with H_2-OH. Nevertheless, the theoretical calculations suggest that the two isotopomers will have similar Boltzmann populations of their rotational levels under equivalent experimental conditions. Instead, the extra lines in the D_2-OH spectrum are more likely due to *o*-D_2-OH, signifying that both nuclear spin states of D_2-OH have been detected.

We have attempted a rigorous assignment of the rotational structure associated with the pure overtone band using repeated combination differences and the theoretically predicted transition frequencies. However, the lack of extended P/R rotational progressions as well as the possibility of overlapping lines from *o*- and *p*-D_2-OH has prevented us from deducing a unique assignment. At least four reasonable rotational assignments can be proposed for the pure overtone band of *p*-D_2-OH. Each of the assignments leaves a few prominent lines unassigned, which is consistent with some transitions arising from *o*-D_2-OH. Therefore, no definitive rotational assignment of the pure overtone band will be presented here.

The combination band appearing at 6981.8 cm^{-1} in the IR spectrum of *o*-H_2-OH has been assigned to overlapping parity components of a Q-branch transition to an excited intermolecular bending state ($K = -1/2$).[29] This assignment was based on the close agreement with theoretical predictions.[13] By analogy, the strong feature at 6983.0 cm^{-1} in the D_2-OH spectrum is ascribed to overlapping Q-branch transitions to an excited bending state ($K = -1/2$) of *p*-D_2-OH, which is also in good accord with the ab initio prediction. Only one strong line is observed for *o*-H_2-OH, while several weaker lines surround the most intense line seen for D_2-OH. Here again, the extra weak lines are likely due to a combination band of *o*-D_2-OH ($K = 1/2 \leftarrow 3/2$), which is expected to exhibit a very large parity splitting.

A detailed comparison of the IR overtone spectra of D_2-OH and H_2-OH (Figure 3) reveals an interesting change in intermolecular energy associated with the first observed combination band on isotopic substitution. The excited bending level ($K = -1/2$) accessed in this transition has an intermolecular energy of 9.9 cm^{-1} in *o*-H_2-OH as compared with 11.0 cm^{-1} in *p*-D_2-OH, indicating a >1 cm^{-1} shift to *higher* energy on deuteration. A similar trend is predicted by theory where the transition frequencies of these combination bands are computed to be 10.0 and 11.3 cm^{-1} for *o*-H_2-OH and *p*-D_2-OH, respectively. This result can be explained in terms of a stronger effective anisotropy for this vibration in D_2-OH compared with H_2-OH because of the reduced zero-point motion in the deuterated isotopomer. Similar arguments have been used to explain an analogous effect in H_2/D_2-HF.[42]

The dynamical studies that are presented in the following sections focus on four different initial states of D_2-OH ($v_{OH} = 2$). Excitation of three strong lines in the pure overtone region,

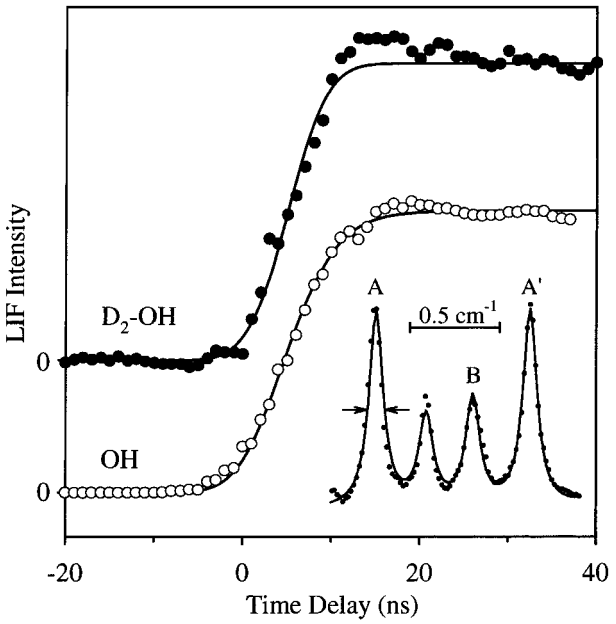

Figure 4. Time- and frequency-domain measurements of the D_2-OH ($\nu_{OH} = 2$) lifetime. The D_2-OH time trace shows the appearance of OH ($v = 1$, $j_{OH} = 9/2$) products following vibrational predissociation. The rise time (≤ 5 ns) is limited by the instrumental time resolution, which is experimentally measured by pumping and probing the OH monomer $v = 2$, $j = 5/2$, $\omega = 3/2$ state as shown in the OH time trace. The inset displays a high-resolution frequency scan of the central portion of the D_2-OH pure overtone band. The homogeneous line width extracted from a fit to the IR spectral data is 0.06 cm^{-1} (fwhm), yielding a 0.09 ns lower limit for the D_2-OH ($\nu_{OH} = 2$) lifetime.

labeled A (6971.8 cm^{-1}), A′ (6972.6 cm^{-1}), and B (6972.3 cm^{-1}) in Figure 3, prepares D_2-OH in low J levels of the ground intermolecular state of *o*-D_2-OH ($K = 3/2$) or *p*-D_2-OH ($K = 1/2$) with two quanta of OH stretch. Excitation of the combination band at 6983.0 cm^{-1}, labeled C in Figure 3, prepares *p*-D_2-OH ($K = -1/2$) in a low J level of an excited intermolecular bending vibration with two quanta of OH stretch. The dramatically different inelastic scattering dynamics observed for these initial states will be used to provide further insight into the characteristics of these states.

B. Lifetime. The lifetime of D_2-OH ($\nu_{OH} = 2$) has been measured directly in the time domain by monitoring the rate of appearance of the OH $X\ ^2\Pi$ ($v = 1$) products from vibrational predissociation. The inverse lifetime derived from this measurement represents the *sum* of the rates for two parallel unimolecular processes, vibrational predissociation and chemical reaction, even though only one of these channels is probed. A typical time trace is shown in Figure 4, which was obtained by varying the time delay between the IR pump and UV probe lasers ($\Delta t = t_{UV} - t_{IR}$). The IR pump laser is fixed on feature A in the pure OH overtone band of D_2-OH and the UV probe laser is fixed on the OH $A-X\ 0-1\ Q_1(9/2)$ transition. No OH LIF signal is observed when the UV probe laser arrives in the interaction region in advance of the IR pump laser. The LIF signal then rises rapidly as the IR pump and UV probe lasers become temporally overlapped, and continues rising to a maximum intensity with a single-exponential time profile.

The instrumental time resolution was evaluated by preparing the OH monomer in the $v = 2$, $j_{OH} = 5/2$ state with the IR pump laser operating on the OH $R_1(3/2)$ transition and probing this same state with the UV laser on the OH $A-X\ 1-2\ Q_1(5/2)$ transition.[33,38] By varying the time interval between the IR pump and UV probe lasers, the lower trace shown in Figure 4 was obtained.

Also shown in Figure 4 are nonlinear least-squares fits to the data using an exponential rise function

$$S(\Delta t) = A[1 - \exp(-\Delta t/\tau)] \quad (1)$$

with unimolecular rate constant $k = 1/\tau$ convoluted over a Gaussian excitation function having a fwhm of 4 ns. The fit to the OH rise time yields an instrumental time resolution of ≤ 5 ns. Similar fits were obtained when the IR pump laser was set to excite D_2-OH features A, A′, and B in the pure overtone region as well as combination band feature C. In each case, the lifetime measurement yielded an upper limit of 5 ns. Therefore, we conclude that D_2-OH ($\nu_{OH} = 2$) decays on a time scale that is less than or equal to the instrumental time resolution.

The lifetime of D_2-OH ($\nu_{OH} = 2$) was also evaluated in the frequency domain using a newly acquired higher resolution OPO as the IR pump source. The higher resolution D_2-OH IR spectrum revealed no additional lines or splittings and was used only for line width measurements. A portion of the high-resolution spectrum between 6971.5 and 6972.9 cm^{-1} is displayed in the inset of Figure 4, which was recorded by action spectroscopy with the probe laser fixed on the OH $A-X\ 0-1\ Q_1(9/2)$ transition. These four lines were well represented by Lorentzian functions with a fwhm of 0.06(1) cm^{-1}, which is only slightly greater than the laser resolution (0.04 cm^{-1}). The fwhm of 0.06 cm^{-1} is taken to be an upper limit to the homogeneous lifetime broadening, because we have not deconvoluted the laser bandwidth nor eliminated the possibility of saturation broadening (reduction of the IR pump power significantly reduces the signal-to-noise ratio and therefore our ability to measure narrower line widths). Thus, we infer that vibrationally activated D_2-OH has a lifetime in excess of 0.090 ns, bracketing the D_2-OH ($\nu_{OH} = 2$) lifetime between 0.090 and 5 ns.

C. OH Product State Distribution. The IR spectrum of D_2-OH shown in Figures 2 and 3 was recorded by action spectroscopy and, as a result, the intensity of each rovibrational transition depends on the IR transition strength as well as the cross section for scattering into the OH product state that is monitored by the UV probe laser. The relative intensities of peaks in the IR action spectrum change dramatically when different probe transitions are monitored (e.g., OH $A-X\ 0-1\ Q_1(9/2)$ versus $P_1(9/2)$ lines), as illustrated in Figure 5. The intensity variation for different OH probe transitions reflects the inelastic scattering dynamics. Note that the transition frequencies are unchanged with different probe transitions.

The IR overtone spectrum of D_2-OH has also been measured by the fluorescence depletion method, as shown in Figure 5, yielding yet another intensity distribution. In this case, the IR pump laser is scanned with the UV probe laser monitoring a D_2-OH electronic transition (feature H′ at 35390 cm^{-1}) in the OH $A-X\ 1-0$ region.[24] The UV probe laser-induced fluorescence signal is depleted each time the IR and UV transitions originate from a common ground-state level. Because the D_2-OH electronic transition exhibits extensive homogeneous line broadening (on the order of 30 cm^{-1}), the UV laser will probe all of the populated rotational levels ($T_{rot} \sim 3$ K) simultaneously and with nearly equal weighting. As a result, the line intensities in the fluorescence depletion spectrum should depend only on the IR transition strength and should closely resemble the IR spectrum that would be obtained by direct absorption.

The remarkably different inelastic scattering dynamics for various initial states of D_2-OH can be readily seen in Figure 5. For example, the dominant line of the pure overtone band in the fluorescence depletion spectrum, feature B, is also prominent

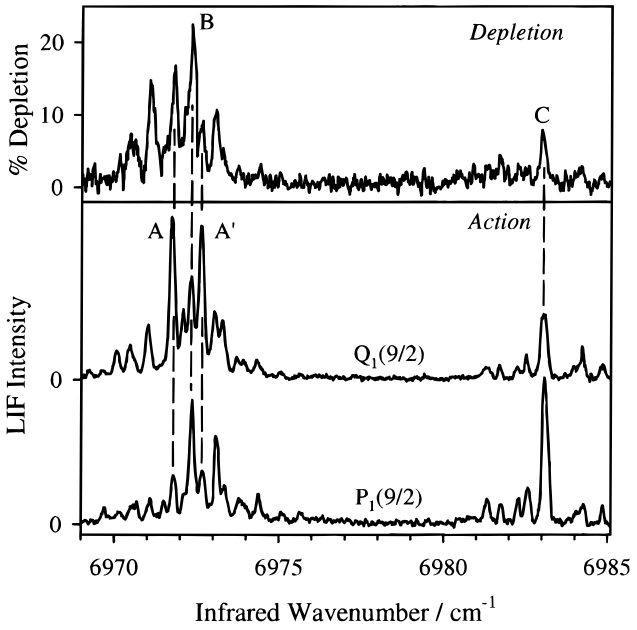

Figure 5. A portion of the IR spectrum of D_2-OH measured via the fluorescence depletion method (upper panel), with the UV probe laser monitoring a D_2-OH electronic transition (feature H′ at 35,390 cm^{-1} in ref 24) in the OH A−X 1−0 region. The bottom panel shows the corresponding region of the D_2-OH IR spectrum recorded via action spectroscopy, with the UV laser probing either the OH A−X 0−1 $Q_1(9/2)$ or $P_1(9/2)$ transition. The vertical dashed lines indicate the IR transitions (features A, A′, B, and C) that are pumped in subsequent dynamical studies.

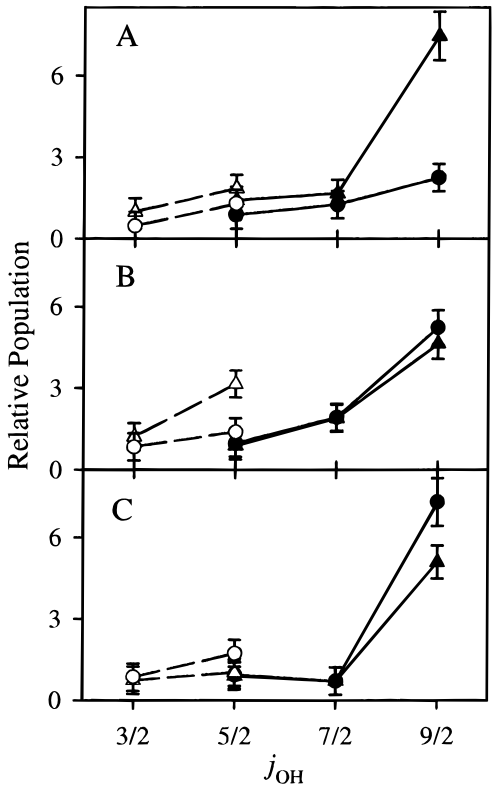

Figure 6. Relative population in OH (v = 1, j_{OH}) product rotational levels on vibrational predissociation of D_2-OH ($\nu_{OH} = 2$) from selected initial states prepared by excitation of features A, B, and C. The filled symbols give the population of the Π(A″) (triangles) and Π(A′) (circles) λ-doublet components in the $\omega = 3/2$ spin−orbit manifold, whereas the open symbols show the corresponding λ-doublet populations in the excited $\omega = 1/2$ spin−orbit manifold.

when the OH $P_1(9/2)$ line is probed in action spectroscopy. Yet feature B is less intense than others; namely, features A and A′, when the OH $Q_1(9/2)$ line is the probe transition. As another example, excitation of a D_2-OH combination band, feature C, preferentially results in OH fragments that are detected on the $P_1(9/2)$ transition, with less seen when the OH $Q_1(9/2)$ line is probed. Feature C is also not as prominent in the fluorescence depletion scan. These intensity changes were not observed in H_2-OH, where IR overtone spectra recorded by fluorescence depletion and action spectroscopy (P- or Q-lines) methods looked much the same.[16,29]

A more direct way to examine the inelastic scattering dynamics is to measure the OH X $^2\Pi$ (v = 1) product state distribution for selected initial states of D_2-OH, specifically, features A, A′, B, and C. Dynamical studies of other weaker lines were not practical because of signal-to-noise considerations. The nascent rotational and fine structure distributions have been evaluated by probing different rotational branches of the OH A−X 0−1 band, using the Dieke and Crosswhite tabulation for identification of transitions.[33] The intensities observed on each of the OH probe transitions were scaled relative to that of the $Q_1(9/2)$ line, which was scanned immediately before and after the measurement of every other line. The experimental measurements of transition intensities were performed in a fully saturated LIF regime (1.5 mJ/pulse excitation energies) and appropriately converted into relative populations of the OH X $^2\Pi$ (v = 1) rotational levels.[16]

The OH (v = 1) product state distributions resulting from excitation of features A, B, and C in the IR spectrum of D_2-OH are shown in Figure 6. Feature A′ yields a nearly indistinguishable product distribution (not shown) from that observed when feature A is pumped. The relative populations of rotor levels in the lower $\omega = 3/2$ spin−orbit manifold are shown as filled symbols, whereas those in the excited $\omega = 1/2$ spin−orbit manifold appear as open symbols. Each OH rotor level is composed of two nearly degenerate λ-doublet states, Π(A″) and Π(A′), denoted by triangles and circles, which have been separately probed by Q and P/R branch transitions, respectively.[43] For all the rotational distributions, the highest energetically accessible rotor state, $j_{OH} = 9/2$, $\omega = 3/2$, is clearly favored, with significantly less population in lower OH rotor states. The population of the lowest rotational level of each spin−orbit manifold, however, could not be determined because of the large background population in these levels. (Cooling of the vibrational and spin−orbit degrees of freedom of the OH monomer is incomplete within the supersonic expansion.)

Significant fine structure effects are observed in the OH (v = 1, j_{OH}) product state distribution. A striking λ-doublet preference is seen when the IR laser pumps feature A (or A′) in the pure overtone region. The Π(A″) λ-doublet component is strongly favored over the Π(A′) component for the $j_{OH} = 9/2$, $\omega = 3/2$ product state. On the other hand, no discernible λ-doublet effect is observed when feature B is excited. By contrast, the *opposite* λ-doublet component, Π(A′), of the $j_{OH} = 9/2$ rotor state is favored when pumping the feature C. The two λ-doublet states of most other rotor states are nearly equally populated. The origin of the λ-doublet preference will be discussed in Section V. E.

By summing over OH rotor levels and λ-doublet states in each spin−orbit manifold, the overall populations in the two spin−orbit states can be compared. After accounting for rotational level degeneracies in both spin−orbit manifolds, a branching ratio between spin−orbit manifolds of 60% ($\omega = 3/2$) to 40% ($\omega = 1/2$) is obtained when pumping the different

D_2-OH features (A, A′, B, and C). Similar branching ratios were also found for the OH ($v = 1$, j_{OH}) products following vibrational predissociation of *o*-H_2-OH with $\nu_{OH} = 2$ and $\nu_{H_2} = 1$.[16,17]

V. Discussion

A. Initial D_2-OH State Selection. Infrared overtone excitation was used to prepare specific rovibrational states of D_2-OH ($\nu_{OH} = 2$) with well-defined energies. Four initial states were chosen for further study in dynamical investigations. Infrared excitation of D_2-OH on three prominent lines in the pure overtone band, labeled features A, A′, and B, prepares D_2-OH ($\nu_{OH} = 2$) in its ground intermolecular state. These transitions are likely low *J* Q-branch transitions, although it is not certain whether they are due to *o*-D_2-OH ($K = 3/2$) or *p*-D_2-OH ($K = 1/2$), because both nuclear spin states are expected to exhibit strong transitions in this spectral region. In addition, a combination band, feature C, accesses an excited intermolecular bending state of *p*-D_2-OH ($\nu_{OH} = 2$) with $K = -1/2$. This transition is also likely to be a low *J* line in the Q-branch. To gain insight into the characteristics of the initial states slated for dynamical investigation, we once again turn to theory. The wave functions associated with the ground intermolecular states of *o*- and *p*-D_2-OH as well as an excited bending state of *p*-D_2-OH (with 11.2 cm^{-1} of intermolecular energy) will be examined to visualize the initial conditions for the half-collision scattering dynamics.

The D_2-OH eigenfunctions computed in Section III using a space-fixed representation must be transformed into the body-fixed frame to explore the angular properties of the wave functions. The mathematical details of this transformation are given elsewhere.[23,44,45] Here, we simply examine the resultant probability amplitude $|\Psi|^2$ as a means of determining the relative orientation of the D_2 and OH subunits within the complex. The four-dimensional D_2-OH wave functions are used to construct one-dimensional polar plots of the D_2 and OH orientations within the complex by integrating over the remaining intermolecular coordinates. The polar angles θ_{D_2} and θ_{OH} are defined as the angle between the diatom bond axis and the intermolecular axis R. Polar plots of the angular probability distributions for D_2 and OH, $|\Psi|^2$ (θ_{D_2}) and $|\Psi|^2$ (θ_{OH}), are displayed adjacent to one another in Figure 7 for three different intermolecular states. The angular probability distributions for the + and − parity components of these three D_2-OH states are indistinguishable, so only the + parity components are shown in Figure 7.

For *o*-D_2-OH in its ground intermolecular state ($K = 3/2$), $|\Psi|^2$ (θ_{D_2}) reveals that the *o*-D_2 diatom is nearly spherical within the complex, illustrating that it is predominantly a $j_{D_2} = 0$ free rotor. The slight asymmetry in the D_2 angular distribution can be traced to a small amount of $j_{D_2} = 2$ character in the wave function. In contrast, $|\Psi|^2$ (θ_{OH}) shows that the OH diatom is oriented along the intermolecular axis with the H end of OH pointing toward D_2 ($\theta_{OH} = 0°$). The angular probability distribution for the OH diatom is consistent with a $j_{OH} = 3/2$, $\omega = 3/2$ free rotor state that has a well-defined projection on the intermolecular axis. In this case, the ground intermolecular state of *o*-D_2-OH exhibits a maximum probability at the T-shaped D_2-HO configuration, which corresponds to the global minimum on the ab initio potential energy surface.[13]

For *p*-D_2-OH in its ground intermolecular state ($K = 1/2$), the shape of the $|\Psi|^2$ (θ_{D_2}) distribution function reveals that the *p*-D_2 diatom is primarily in a $j_{D_2} = 1$ free rotor state with the D_2 molecule aligned perpendicular to the intermolecular axis ($\theta_{D_2} = 90°$). The distribution shows that the OH diatom is also aligned nearly perpendicular to the intermolecular axis. The angular probability distribution for the OH diatom is indicative of a $j_{OH} = 3/2$, $\omega = 3/2$ free rotor state with a well-defined projection on the intermolecular axis. Thus, the peak of the probability distribution for the ground state of *p*-D_2-OH occurs with the D_2 and OH diatoms in a near parallel configuration, which is significantly different than that found for the ground state of *o*-D_2-OH.

Finally, the $|\Psi|^2$ (θ_{D_2}) distribution function for *p*-D_2-OH in the excited intermolecular bending state ($K = -1/2$) shows that *p*-D_2 is still in a $j_{D_2} = 1$ free rotor state, but with the D_2 molecule aligned *along* the intermolecular axis ($\theta_{D_2} = 0°$). From $|\Psi|^2$ (θ_{OH}), it is evident that the OH diatom spatial distribution is essentially unchanged from the ground *p*-D_2-OH state. Again,

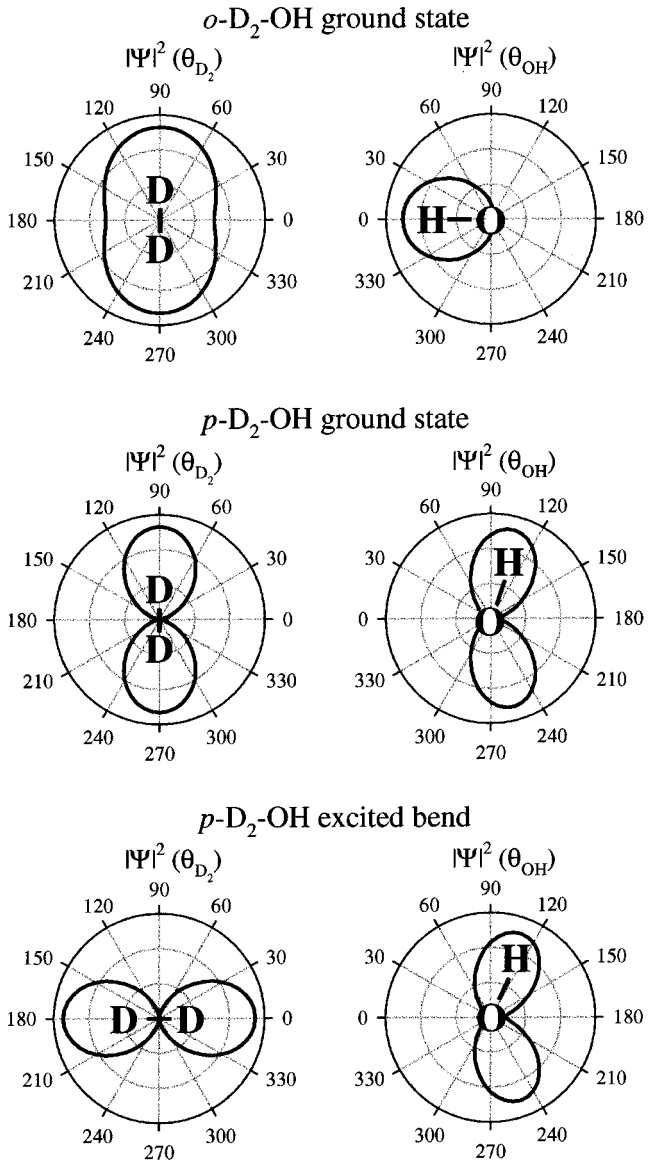

Figure 7. Polar plots of the D_2 and OH angular probability distributions from quantum calculations on the MCKW ab initio potential (ref 13). The angles θ_{D_2} and θ_{OH} are defined as zero for a linear D−D−H−O configuration. The relative orientations of the D_2 and OH partners within the complex are dramatically different for the selected intermolecular states of *o*- and *p*-D_2-OH. The ground state of *o*-D_2-OH is predicted to be T-shaped, the ground state of *p*-D_2-OH has a parallel configuration for the D_2 and OH diatoms, and the excited intermolecular bend of *p*-D_2-OH has an L-shaped structure reminiscent of the transition state to reaction.

the OH angular distribution is consistent with a $j_{OH} = 3/2$, $\omega = 3/2$ free rotor state. The maximum in the probability distribution for *p*-D_2−OH in this excited intermolecular bending state occurs in an L-shaped configuration. This L-shaped configuration is very similar to the orientation of the diatoms at the transition state to reaction.[7,46,47] Thus, we see that intermolecular bending excitation can dramatically change the relative orientation of the partners within the D_2−OH complex. The ramifications of these distinctly different structures on the inelastic scattering dynamics of D_2−OH are explored in Section E of the discussion.

B. Lifetime of Vibrationally Activated D_2−OH. The D_2−OH ($\nu_{OH} = 2$) complex contains ~6972 cm^{-1} of energy, with the excitation initially localized in the intramolecular stretching vibration of the OH partner. Consequently, both reaction and vibrational predissociation are energetically accessible decay channels. However, the OH bond is generally viewed as a "spectator" to the OH + H_2/D_2 reaction.[46,48] As a result, vibrational excitation of the OH partner in D_2−OH is not expected to promote the reactive channel significantly. Similarly, the OH vibration is not expected to strongly couple to the vibrational predissociation channel because of the mismatch between the high-frequency OH stretch and low-frequency intermolecular vibrations.[15,29]

The lifetimes measured for D_2−OH, bracketed in this work between 0.090 and 5 ns, reflect the time it takes the excited OH stretch to couple to the vibrational predissociation and/or reaction coordinates. The lifetime of *o*-H_2−OH ($\nu_{OH} = 2$) has previously been determined to be 115(26) ns.[29] Therefore, isotopic substitution results in at least a 20-fold increase in the decay rate.

Previous studies of vibrational predissociation in closed-shell systems, such as H_2/D_2−HF, have shown that the rate of vibrational predissociation can be significantly enhanced when a V−V energy transfer pathway is available. For example, Nesbitt and co-workers found a reduction in lifetime from 27 to 1.12 ns upon deuteration.[40,41] The V−V channel is open for D_2−HF, but energetically closed for H_2−HF. The V−V pathway minimizes the translational energy of the product molecules, which is a key factor for efficient predissociation according to energy and momentum gap laws.[49−52] Several theoretical calculations have verified that the opening of the V−V channel accounts for the significantly reduced lifetime of D_2−HF as compared to H_2−HF.[42,53−55]

The experimental results for D_2−OH ($\nu_{OH} = 2$) are in good agreement with the theoretical predictions of Krause et al.,[15] who carried out time-dependent wave packet calculations to obtain vibrational predissociation lifetimes of 1.6 ns for *o*-D_2−OH ($\nu_{OH} = 2$) and 0.15 ns for *p*-D_2−OH ($\nu_{OH} = 2$). Krause et al.[15] also predicted a vibrational predissociation lifetime for *o*-H_2−OH ($\nu_{OH} = 2$) of 210 ns, which is also in good accord with experiment. Note that the theoretical calculations considered only the vibrational predissociation channel and did not take into account the possibility of reaction. The significant change in the computed vibrational predissociation rate indicates that the two isotopomers undergo qualitatively different decay dynamics. Vibrational predissociation of H_2−OH proceeds via a relatively slow and inefficient V−R,T mechanism.[15,16] The ~3350 cm^{-1} of energy that is released from one quantum of OH stretch is not sufficient to vibrationally excite the H_2 partner (4155 cm^{-1}). On the other hand, vibrational predissociation of D_2−OH ($\nu_{OH} = 2$) follows a V−V mechanism that transfers one quantum of vibrational excitation from OH to D_2 and provides a relatively efficient decay channel.[15]

Based on the theoretical calculations, it appears that much of the decrease in lifetime of vibrationally activated D_2−OH compared with H_2−OH results from an increase in the rate of vibrational predissociation. Nevertheless, one cannot discount the possibility that reaction contributes to the decay dynamics of D_2−OH ($\nu_{OH} = 2$). The V−V mechanism could enhance the rates for *both* vibrational predissociation and reaction because the V−V process provides an indirect way to vibrationally activate D_2. Kinetic studies have shown a >100-fold increase in the rate of reaction when H_2 is vibrationally excited,[30,31] whereas vibrational excitation of OH does not enhance the rate of reaction significantly.[48] Furthermore, theoretical calculations have also shown that the probability of reaction is enhanced and the threshold for reaction is substantially reduced (to nearly zero) on vibrational excitation of H_2.[5,56,57]

C. Product State Distribution. In this section, we determine the combinations of OH (v = 1) and D_2 (v = 1) fragment rotational states (j_{OH}, j_{D_2}) that are populated following vibrational predissociation of D_2−OH ($\nu_{OH} = 2$) from three different initial states. In each case, the OH (v = 1) fragment rotational and fine structure states have been evaluated directly (Figure 6). Although the D_2 (v = 1) fragments have not been probed, it is still possible to determine which D_2 rotor levels are populated based on energetic constraints. We assume that the rate of interconversion between *o*- and *p*-D_2 within the D_2−OH complex is negligibly small on the time scale of the experiments. This assumption ensures that only *o*-D_2 fragments are produced following vibrational predissociation of *o*-D_2−OH and, similarly, that only *p*-D_2 fragments are formed on predissociation of *p*-D_2−OH. The rotational states of the D_2 (v = 1) fragments that can be populated along with each observed OH (v = 1, j_{OH}) channel can then be determined using an energy cycle.

Because the pure overtone lines (features A, A′, and B) can be due to *o*- or *p*-D_2−OH, we consider both possibilities. As shown in Figure 1 (enlargement), only two D_2 rotor states can be populated on vibrational predissociation of *p*-D_2−OH because of the relatively small amount of energy that is imparted to the OH (v = 1) + D_2 (v = 1) products. In particular, only the $j_{D_2} = 1$ product state can be populated for $j_{OH} = 9/2$, 7/2, and 5/2, with $\omega = 3/2$, as well as for $j_{OH} = 5/2$, 3/2, and 1/2, with $\omega = 1/2$. The near resonant (j_{OH}, j_{D_2}) = (9/2, 1) channel leaves only 4 cm^{-1} in translational energy of the recoiling fragments. Excitation of the combination band of *p*-D_2−OH (feature C) does not access any additional product channels. Similarly, pure overtone excitation of *o*-D_2−OH results in $j_{D_2} = 0$ exclusively for $j_{OH} = 9/2$ and 7/2, with $\omega = 3/2$, as well as for $j_{OH} = 5/2$, with $\omega = 1/2$. Thus, the OH fragment acquires most of the available energy as rotational excitation in the predominant product channel.

The time-dependent wave packet calculations of Krause et al.[15] also yield the product state distribution of the OH and D_2 fragments following vibrational predissociation of *o*- and *p*-D_2−OH ($\nu_{OH} = 2$). The calculations were performed using the MCKW ab initio potential,[13] but did not take into account the open-shell nature of OH because of computational limitations. Nevertheless, the agreement between experiment and theory is good on a qualitative level for *o*- and *p*-D_2−OH. Both experiment and theory give product OH and D_2 excited in a small number of rotational states just below the resonance energy (the maximum energy available for products) for the V−V channel. In addition, both experiment and theory show that the highest energetically accessible (j_{OH}, j_{D_2}) channel is populated with the highest probability.

D. Orbital Alignment. Vibrational predissociation of D_2-OH ($\nu_{OH} = 2$) results in significant fine structure effects in the OH ($v = 1$, j_{OH}) product state distribution. Specifically, a striking λ-doublet preference is seen in the most near resonant $j_{OH} = 9/2$, $\omega = 3/2$ product state that depends on the initial state of D_2-OH prepared with the IR laser. The λ-doublet preference reveals that the unpaired pπ orbital of the OH fragment is aligned with respect to the OH rotation plane. The degree of electron alignment (DEA) is commonly evaluated according to $[\Pi(A'') - \Pi(A')]/[\Pi(A'') + \Pi(A')]$.[58,59] Here, $\Pi(A'')$ and $\Pi(A')$ are the populations of the two λ-doublet components. In the high j_{OH} limit (Hund's case b), the unpaired pπ orbital of OH is aligned perpendicular to the OH rotation plane for the $\Pi(A'')$ λ-doublet component, whereas the unpaired pπ lobe lies in the OH rotation plane for the $\Pi(A')$ component.

For low-to-moderate j_{OH}, including $j_{OH} = 9/2$, $\omega = 3/2$, the unpaired pπ orbital alignment associated with the two λ-doublet components is incomplete, as a result of mixed Hund's case a and b coupling. The intrinsic electronic wave function mixing can be factored out of the experimentally derived DEA, as described in ref 16, yielding a quantity known as the reduced DEA.[60] The reduced DEA then reveals the degree of alignment arising solely from the predissociation dynamics. A reduced DEA of $+1$ implies complete pπ orbital alignment perpendicular to the OH rotation plane, whereas a value of -1 indicates complete orbital alignment within the OH rotation plane. A reduced DEA of zero shows no alignment.

Dramatically different values of reduced DEA are obtained from each of the initially prepared D_2-OH ($\nu_{OH} = 2$) states. Excitation of the ground intermolecular state of D_2-OH ($\nu_{OH} = 2$) on feature A (or A′) results in a reduced DEA value of 0.9 ± 0.2 (or 0.8 ± 0.2) for the $j_{OH} = 9/2$, $\omega = 3/2$ product state. These values are quite close to the limiting value of 1, which implies complete alignment of the unpaired pπ orbital perpendicular to the OH rotation plane resulting from the dynamical event. By contrast, pure overtone excitation of D_2-OH on feature B yields a reduced DEA of -0.1 ± 0.2 for the same product state, indicating little or no alignment of the OH pπ orbital. Finally, preparation of the excited intermolecular bending state of p-D_2-OH ($\nu_{OH} = 2$) on feature C yields a reduced DEA of -0.3 ± 0.2, showing partial alignment of the OH pπ orbital in the opposite sense, that is, within the OH rotation plane. Possible origins for this dynamical alignment effect will be discussed in the next section.

The strong λ-doublet preference is seen primarily for one OH product state, $j_{OH} = 9/2$, $\omega = 3/2$, whereas most other product channels have nearly equal population for the two λ-doublet states. The very small kinetic energy released to the fragments for the (j_{OH}, j_{D_2}) = (9/2, 1) and (9/2, 0), channels may account for the enhanced λ-doublet preference. Similarly, in full-collision studies of OH + H_2 and CH + He/D_2, fine structure effects were far more prominent for product channels where most of the available energy was disposed in rotational excitation of the products.[11,60,61] When product translational energy is minimized, the products recoil from one another slowly and therefore spend more time under the influence of the attractive regions of the potential.

E. Half-Collision Scattering Dynamics. Vibrational predissociation of D_2-OH ($\nu_{OH} = 2$) is analogous to the second half of an inelastic scattering event. Both full- and half-collisions of OH X $^2\Pi$ with D_2 are complicated by the presence of two adiabatic potential energy surfaces in the entrance channel.[13,62,63] These surfaces are denoted as $V_{A''}$ and $V_{A'}$ for planar configurations, depending on whether the OH unpaired pπ orbital lies perpendicular to or in the collision plane, respectively. The potentials are nearly degenerate in the OH X $^2\Pi$ + H_2/D_2 asymptotic limit, but split apart from one another as the reactants approach each other in nonlinear configurations. Only the $V_{A'}$ surface with the unpaired pπ orbital in plane can lead to reaction for favorable orientations of the partners.[46] The scattering process is typically described in the diabatic representation,[10,13,64] with the dynamics occurring on the average $V_{AVG} = (V_{A''} + V_{A'})/2$ and difference $V_{DIF} = (V_{A''} - V_{A'})/2$ potentials.

In full collisions of OH X $^2\Pi$ with n- and p-H_2, the λ-doublet states of the inelastically scattered OH products were found to be unequally populated.[9,11,14] A preference for the $\Pi(A')$ λ-doublet component was observed when the initial OH λ-doublet states were equally populated and, to some extent, when starting from even a single λ-doublet state. Theoretical studies have traced the unequal λ-doublet populations to quantum interference effects between scattering amplitudes arising from the V_{AVG} and V_{DIF} surfaces.[10,65] More generally, in full collisions of a $^2\Pi$ radical with a spherically symmetric partner, Dagdigian et al.[65] have shown that the relative signs of V_{DIF} and V_{AVG} determine which λ-doublet state should be favored in inelastic scattering.

Like the full collision studies, the OH ($v = 1$) products from vibrational predissociation of D_2-OH ($\nu_{OH} = 2$) show a significant λ-doublet preference in the near resonant $j_{OH} = 9/2$, $\omega = 3/2$ final state. Surprising, however, is the enormous variation in the alignment of the unpaired pπ orbital with respect to the OH rotation plane (as reflected by the λ-doublet preference) that is observed for different initial rovibrational states of D_2-OH. Most striking is the change in pπ orbital alignment upon intermolecular bending excitation. Significant changes are also seen for ground intermolecular states (features A, A′, and B) of D_2-OH even though energy differences between these states are very small. Clearly, the distinct initial states of D_2-OH ($\nu_{OH} = 2$) are strongly influencing the half-collision inelastic scattering dynamics.

By analogy with the full collision results, the λ-doublet preference seen in the vibrational predissociation dynamics likely originates from the same quantum interference phenomenon. Ab initio calculations indicate that the D_2-OH difference potential V_{DIF} is highly anisotropic, changing in both *magnitude* and *sign* as a function of the orientation of the partners.[13] These changes in V_{DIF} are evident in the top panel of Figure 8, which shows one-dimensional cuts of V_{DIF} as a function of the orientation of the D_2 partner (θ_{D_2}) with OH positioned at a perpendicular ($\theta_{OH} = 90°$) or linear ($\theta_{OH} = 0°$) orientation and R fixed at 3.2 Å. In general, V_{DIF} is large in magnitude for $\theta_{OH} = 90°$ as the OH pπ orbital points toward D_2. Nevertheless, V_{DIF} still varies in sign and magnitude as the D_2 partner is rotated, ranging from strongly positive at $\theta_{D_2} = 90°$ to negative at 0° (or 180°). By contrast, when OH is positioned along the intermolecular axis ($\theta_{OH} = 0°$), V_{DIF} is nearly zero (with little change as θ_{D_2} is varied) because the OH pπ orbital lies perpendicular to the intermolecular axis. Of course, V_{AVG} is negative (attractive) throughout the bound region of the potential.

The D_2 angular probability distribution $|\Psi|^2$ (θ_{D_2}) for o-D_2-OH in its ground intermolecular state is plotted in a similar format in the middle panel of Figure 8. (Polar plots of $|\Psi|^2$ (θ_{D_2}) are given in Figure 7.) Figure 8 shows a broad angular distribution that is centered at $\theta_{D_2} = 90°$. This state accesses a region of the potential where V_{DIF} is nearly zero, because OH is oriented along the intermolecular axis ($\theta_{OH} \sim 0°$). As a result, the ground intermolecular state of o-D_2-OH is not expected to

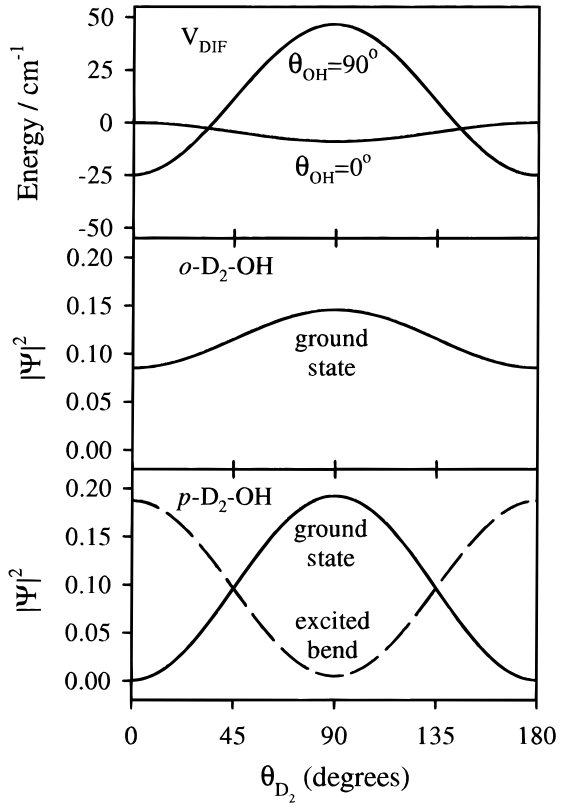

Figure 8. Angular dependence of the difference potential (V_{DIF}) from MCKW ab initio potential (ref 13) and corresponding D_2 angular probability distributions for *o*- and *p*-D_2−OH in selected intermolecular states. Although V_{DIF} is nearly isotropic in the region accessed by the ground state of *o*-D_2−OH ($\theta_{OH} = 0°$), the magnitude and sign of V_{DIF} changes for the regions of the potential sampled by the ground state and excited bend of *p*-D_2−OH ($\theta_{OH} = 90°$).

give rise to a significant OH pπ orbital alignment in its inelastic scattering dynamics.

Analogous D_2 angular probability distributions $|\Psi|^2$ (θ_{D_2}) for *p*-D_2−OH in its ground state and excited bending state are plotted in the bottom panel of Figure 8. The peak amplitude for *p*-D_2−OH occurs at $\theta_{D_2} = 90°$ in its ground state, whereas in the excited bending state it has a minimum at $\theta_{D_2} = 90°$, with maximal values at $\theta_{D_2} = 0°$ and 180°. Because OH is oriented nearly perpendicular to the intermolecular axis in these states ($\theta_{OH} \sim 90°$), the ground intermolecular state samples regions of the potential where V_{DIF} is strongly positive and the excited bending state accesses regions where V_{DIF} is negative. Consequently, the interference terms and the resultant pπ orbital alignment[65] of the OH fragments from vibrational predissociation should be different, favoring the $\Pi(A'')$ λ-doublet state for the ground intermolecular state of *p*-D_2−OH and the $\Pi(A')$ λ-doublet state for the excited intermolecular bending state of *p*-D_2−OH. (These arguments assume a planar dissociation mechanism.)

Experimentally, we find that the $\Pi(A')$ λ-doublet state is indeed preferred (Figure 6) following excitation of the intermolecular bending state at 11.2 cm^{-1}. This result is consistent with our spectroscopic assignment of feature C as an excited bending state ($K = -1/2$) of *p*-D_2−OH. The λ-doublet propensities also suggest possible assignments for features A, A′, and B in the pure overtone region. Features A and A′ likely access the ground intermolecular state of *p*-D_2−OH ($K = 1/2$) as evidenced by the strong preference to populate the OH $\Pi(A'')$ λ-doublet state. Feature B may be due to the ground intermolecular state of *o*-D_2−OH ($K = 3/2$) because no λ-doublet preference is observed.

The tentative assignments deduced from the inelastic scattering studies are consistent with the appearance of the IR spectrum for D_2−OH. The magnitude and sign of V_{DIF} gives rise to a splitting between states with the same *J* but opposite parity.[13,23] The ground intermolecular state of *o*-D_2−OH accesses a region of the potential where V_{DIF} is nearly zero and, therefore, this state will exhibit a negligibly small parity splitting. As a result, the two parity components of each rotor line will be overlapped in the pure overtone band. The strength of feature B in the fluorescence depletion spectrum (the experimental method closest to direct absorption) may be attributed to overlapping parity components of the Q-branch in *o*-D_2−OH. On the other hand, the ground intermolecular state of *p*-D_2−OH samples regions of the potential where V_{DIF} is strongly positive, and the resultant parity splitting is predicted to be large. This large splitting will give rise to two resolvable parity components for each rotational line in the pure overtone band. Features A and A′ are probably two different parity components of a Q-branch line (low *J*) in *p*-D_2−OH. Therefore, both *o*- and *p*-D_2−OH are likely to have been observed in the pure OH overtone region of the IR spectrum.

VI. Conclusions

This paper reports the rotationally resolved IR spectrum of D_2−OH in the OH overtone region, consisting of the pure OH stretch and combination bands involving intermolecular bending excitation. The analysis of the experimental spectrum has been guided by theoretical predictions of the transition frequencies, which have been deduced from bound state calculations of the rovibrational energy levels. The angular properties of the wave functions have also been explored to visualize the relative orientation of the D_2 and OH diatoms in selected initial states. The ground intermolecular state of *o*-D_2−OH is predicted to have a T-shaped vibrationally averaged structure, whereas *p*-D_2−OH has the D_2 and OH diatoms aligned parallel to one another in its ground state. An excited intermolecular bending state of *p*-D_2−OH favors an L-shaped configuration that is reminiscent of the transition state for reaction.

The vibrationally activated *o*-D_2−OH and *p*-D_2−OH complexes in the $\nu_{OH} = 2$ state are short-lived, with lifetimes bracketed between 0.090 and 5 ns by frequency- and time-resolved measurements. The rapid decay of the initial state is attributed, at least in part, to an efficient near-resonant vibration-to-vibration energy transfer process that results in predissociation of the complex into OH ($v = 1$, j_{OH}) + D_2 ($v = 1$, j_{D_2}). The vibrational energy transfer process moves the initial excitation from the OH bond, which is a spectator to reaction, into the D_2 bond that evolves into the reaction coordinate. The possibility that reaction also contributes to the rapid decay cannot be ruled out from the present work that probes only the products of vibrational predissociation. Ongoing experiments in this laboratory will attempt to detect the D atom products from chemical reaction.

The vibrational predissociation dynamics of D_2−OH ($\nu_{OH} = 2$) from four different initial intermolecular states has been explored in depth. In each case, most of the 350 cm^{-1} of available energy is disposed as OH rotational excitation with the D_2 partner remaining in its lowest rotational level. The relative population of the OH λ-doublet components in the near-resonant $j_{OH} = 9/2$, $\omega = 3/2$ product state reveals a striking λ-doublet preference that changes with initial state. The OH λ-doublet preferences indicate that the unpaired pπ orbital can

be strongly aligned perpendicular to the OH rotation plane, have little or no orbital alignment, or be partially aligned within the OH rotation plane. The pπ orbital alignment reflects the magnitude and sign of V_{DIF} in the region of the potential sampled by each intermolecular state. Theoretical calculations of the inelastic scattering dynamics are needed to confirm the origin of the pπ orbital alignment.

Acknowledgment. This work was supported by grants from the Chemistry Division of the National Science Foundation and the Office of Basic Energy Sciences of the Department of Energy. The authors thank Steven M. Miller and David C. Clary (University College, London) for supplying us with their 4D bound state code for H_2-OH.

References and Notes

(1) Wayne, R. P. *Chemistry of Atmospheres: An Introduction to the Chemistry of the Atmospheres of Earth, the Planets, and their Satellites*, 2nd ed.; Oxford University Press: Oxford, 1991.
(2) Glassman, I. *Combustion*, 3rd ed.; Academic Press: San Diego, 1996.
(3) Clary, D. C. *J. Chem. Phys.* **1992**, *96*, 3656.
(4) Zhang, D. H.; Zhang, J. Z. H. *J. Chem. Phys.* **1993**, *99*, 5615.
(5) Zhang, D. H.; Zhang, J. Z. H. *J. Chem. Phys.* **1994**, *101*, 1146.
(6) Alagia, M.; Balucani, N.; Casavecchia, P.; Stranges, D.; Volpi, G. G. *J. Chem. Phys.* **1993**, *98*, 2459.
(7) Alagia, M.; Balucani, N.; Casavecchia, P.; Stranges, D.; Volpi, G. G.; Clary, D. C.; Kliesch, A.; Werner, H.-J. *Chem. Phys.* **1996**, *207*, 389.
(8) Clary, D. C. *Science* **1998**, *279*, 1879.
(9) Andresen, P.; Häusler, H.; Lülf, H. W. *J. Chem. Phys.* **1984**, *81*, 571.
(10) Schinke, R.; Andresen, P. *J. Chem. Phys.* **1984**, *81*, 5644.
(11) Andresen, P.; Aristov, N.; Beushausen, V.; Häusler, D.; Lülf, H. W. *J. Chem. Phys.* **1991**, *95*, 5763.
(12) Offer, A. R.; van Hemert, M. C.; van Dishoeck, E. F. *J. Chem. Phys.* **1994**, *100*, 362.
(13) Miller, S. M.; Clary, D. C.; Kliesch, A.; Werner, H.-J. *Mol. Phys.* **1994**, *83*, 405.
(14) Schreel, K.; ter Meulen, J. J. *J. Chem. Phys.* **1996**, *105*, 4522.
(15) Krause, P. J.; Clary, D. C.; Anderson, D. T.; Todd, M. W.; Schwartz, R. L.; Lester, M. I. *Chem. Phys. Lett.* **1998**, *294*, 518.
(16) Hossenlopp, J. M.; Anderson, D. T.; Todd, M. W.; Lester, M. I. *J. Chem. Phys.* **1998**, *109*, 10707.
(17) Wheeler, M. D.; Todd, M. W.; Anderson, D. T.; Lester, M. I. *J. Chem. Phys.* **1999**, *110*, 6732.
(18) Wheeler, M. D.; Anderson, D. T.; Todd, M. W.; Lester, M. I.; Krause, P. L.; Clary, D. C. *Mol. Phys.* **1999**, *97*, 151.
(19) Zhao, Z. Q.; Chapman, W. B.; Nesbitt, D. J. *J. Chem. Phys.* **1995**, *102*, 7046.
(20) Zhao, Z. Q.; Chapman, W. B.; Nesbitt, D. J. *J. Chem. Phys.* **1996**, *104*, 3555.
(21) Hawthorne, G.; Sharkey, P.; Smith, I. W. M. *J. Chem. Phys.* **1998**, *108*, 4693.
(22) Lendvay, G.; Bradley, K. S.; Schatz, G. C. *J. Chem. Phys.* **1999**, *110*, 2963.
(23) Miller, S. M.; Clary, D. C. *J. Chem. Phys.* **1993**, *98*, 1843.
(24) Loomis, R. A.; Lester, M. I. *J. Chem. Phys.* **1995**, *103*, 4371.
(25) Loomis, R. A.; Schwartz, R. L.; Lester, M. I. *J. Chem. Phys.* **1996**, *104*, 6984.
(26) Loomis, R. A.; Lester, M. I. *Annu. Rev. Phys. Chem.* **1997**, *48*, 643.
(27) Lester, M. I.; Loomis, R. A.; Schwartz, R. L.; Walch, S. P. *J. Phys. Chem. A* **1997**, *101*, 9195.
(28) Schwartz, R. L.; Anderson, D. T.; Todd, M. W.; Lester, M. I. *Chem. Phys. Lett.* **1997**, *273*, 18.
(29) Anderson, D. T.; Schwartz, R. L.; Todd, M. W.; Lester, M. I. *J. Chem. Phys.* **1998**, *109*, 3461.
(30) Glass, G. P.; Chaturvedi, B. K. *J. Chem. Phys.* **1981**, *75*, 2749.
(31) Zellner, R.; Steinert, W. *Chem. Phys. Lett.* **1981**, *81*, 568.
(32) Toth, R. A.; Margolis, J. S. *J. Mol. Spectrosc.* **1975**, *55*, 229.
(33) Dieke, G. H.; Crosswhite, H. M. *J. Quant. Spectrosc. Radat. Transfer* **1962**, *2*, 97.
(34) Brannon, P. J.; Church, C. H.; Peters, C. W. *J. Mol. Spec.* **1968**, *27*, 44.
(35) Green, W. H., Jr.; Lester, M. I. *J. Chem. Phys.* **1992**, *96*, 2573.
(36) Chakravarty, C.; Clary, D. C. *J. Chem. Phys.* **1991**, *94*, 4149.
(37) Dubernet, M.-L.; Flower, D.; Hutson, J. M. *J. Chem. Phys.* **1991**, *94*, 7602.
(38) Coxon, J. A. *Can. J. Phys.* **1980**, *58*, 933.
(39) The center-of-gravity was determined from the fluorescence depletion measurement described in Section IV. C.
(40) Lovejoy, C. M.; Nelson, D. D., Jr.; Nesbitt, D. J. *J. Chem. Phys.* **1987**, *87*, 5621.
(41) Lovejoy, C. M.; Nelson, D. D., Jr.; Nesbitt, D. J. *J. Chem. Phys.* **1988**, *89*, 7180.
(42) Clary, D. C.; Knowles, P. J. *J. Chem. Phys.* **1990**, *93*, 6334.
(43) Alexander, M. H.; Andresen, P.; Bacis, R.; Bersohn, R.; Comes, F. J.; Dagdigian, P. J.; Dixon, R. N.; Field, R. W.; Flynn, G. W.; Gericke, K.-H.; Grant, E. R.; Howard, B. J.; Huber, J. R.; King, D. S.; Kinsey, J. L.; Kleinermanns, K.; Kuchitsu, K.; Luntz, A. C.; McCaffery, A. J.; Pouilly, B.; Reisler, H.; Rosenwaks, S.; Rothe, E. W.; Shapiro, M.; Simons, J. P.; Vasudev, R.; Wiesenfeld, J. R.; Wittig, C.; Zare, R. N. *J. Chem. Phys.* **1988**, *89*, 1749.
(44) Launay, J. M. *J. Phys. B* **1977**, *10*, 3665.
(45) Anderson, D. T.; Lester, M. I., manuscript in preparation.
(46) Walch, S. P.; Dunning, T. H. *J. Chem. Phys.* **1980**, *72*, 1303.
(47) Isaacson, A. D. *J. Chem. Phys.* **1997**, *107*, 3832.
(48) Spencer, J. E.; Endo, H.; Glass, G. P. Reactions of Vibrationally Excited OH. In *Sixteenth Symposium (Int.) on Combustion*; The Combustion Institute: Pittsburgh, 1976; p 829.
(49) Beswick, J. A.; Jortner, J. *Adv. Chem. Phys.* **1981**, *47*, 363.
(50) Ewing, G. E. *J. Chem. Phys.* **1979**, *71*, 3143.
(51) Ewing, G. E. *Faraday Discuss. Chem. Soc.* **1982**, *73*, 325.
(52) Ewing, G. E. *J. Phys. Chem.* **1987**, *91*, 4662.
(53) Clary, D. C. *J. Chem. Phys.* **1992**, *96*, 90.
(54) Zhang, D. H.; Zhang, J. Z. H.; Bacic, Z. *J. Chem. Phys.* **1992**, *97*, 3149.
(55) Krause, P. J.; Clary, D. C. *Mol. Phys.* **1998**, *93*, 619.
(56) Schatz, G. C. *J. Chem. Phys.* **1981**, *74*, 1133.
(57) Truong, T. N. *J. Chem. Phys.* **1995**, *102*, 5335.
(58) Andresen, P.; Ondrey, G. S.; Titze, B.; Rothe, E. W. *J. Chem. Phys.* **1984**, *80*, 2548.
(59) Andresen, P.; Rothe, E. W. *J. Chem. Phys.* **1985**, *82*, 3634.
(60) Macdonald, R. G.; Liu, K. *J. Chem. Phys.* **1989**, *91*, 821.
(61) Macdonald, R. G.; Liu, K. *J. Chem. Phys.* **1990**, *93*, 2431.
(62) Kochanski, E.; Flower, D. R. *Chem. Phys.* **1981**, *57*, 217.
(63) Offer, A. R.; van Hemert, M. C. *J. Chem. Phys.* **1993**, *99*, 3836.
(64) Alexander, M. H. *J. Chem. Phys.* **1982**, *76*, 5974.
(65) Dagdigian, P. J.; Alexander, M. H.; Liu, K. *J. Chem. Phys.* **1989**, *91*, 839.